Journal of Alloys and Compounds 791 (2019) 184–192

Contents lists available at ScienceDirect

Journal of Alloys and Compounds

journal homepage: http://www.elsevier.com/locate/jalcom

Cu@Au self-assembled nanoparticles as SERS-active substrates for (bio)molecular sensing

Gema Cabello [a, *], Kenneth C. Nwoko [b], José F. Marco [c], María Sánchez-Arenillas [c], Ana María Méndez-Torres [d], Jorg Feldmann [b], Claudia Yáñez [d], Tim A.D. Smith [a, **]

[a] School of Medicine, Medical Sciences and Nutrition, University of Aberdeen, Foresterhill, Aberdeen AB25 2ZD, United Kingdom
[b] Department of Chemistry, School of Natural and Computing Sciences, University of Aberdeen, Aberdeen AB24 3UE, UK
[c] Instituto de Química-Física "Rocasolano"-CSIC, c/ Serrano, 119, 28006, Madrid, Spain
[d] Centro de Investigación de Procesos Redox, Facultad de Ciencias Químicas y Farmacéuticas, Universidad de Chile, Santiago, Chile

ARTICLE INFO

Article history:
Received 30 January 2019
Received in revised form
18 March 2019
Accepted 19 March 2019
Available online 20 March 2019

Keywords:
Biochemical sensing
SERS substrate
Bimetallic nanoparticles
Microwave-assisted heating
Core-shell

ABSTRACT

Cu^0(core)-Au^0(shell) (Cu@Au) bimetallic nanoparticles (NPs) synthesized under microwave-assisted heating were interrogated for surface enhanced Raman scattering (SERS)-active substrates. NPs characterization, by XRD, XPS and UV/vis spectroscopy, showed the formation of self-assembled particles with the occurrence of electron transfer from Cu to Au and the absence of Cu_xO. TEM and AF4 demonstrated NPs with a mean diameter of 4.7 nm. Despite the low LSPR shown by small nanoparticles (<10 nm diameter), our Cu@Au NPs showed enhanced SERS effect, demonstrated by the calculated scattering signal enhancement factor (3×10^5), which may be related to electromagnetic coupling. Selected examples of analytes of interest, including some biomolecules, were studied to demonstrate the versatility of our Cu@Au NPs as SERS-active substrates.

1. Introduction

Nanotechnology has unquestionably crossed many scientific research fields, contributing to the interdisciplinary nature of Science. Over the past twenty years there has been much attention paid to the synthesis and application of single metal nanoparticles (NPs) in the fields of analytical chemistry, catalysis, medicine, etc. More recently, there is increasing interest in the singular properties of alloyed and/or bimetallic nanomaterials. In particular, unique physico-chemical properties of metallic nanomaterials as SERS substrates have led to rapid progress in analytical sensing. Raman scattering has emerged as a powerful technique for chemical sensing facilitating the detection of target molecules at trace levels and has demonstrated utility for use with biological samples such as tissues and living cells [1]. However, the performance of SERS substrates based on bimetallic NPs strongly depends on their morphological and structural properties (as a direct consequence of electromagnetic coupling), which are unequivocally controlled by the preparation method [2,3]. The development of SERS substrates with a high surface-to-volume ratio able to generate hot spots has become one of the primary goals in the advancement of analytical sensors. Small NP (<10 nm diameter) colloids show weak surface plasmon resonance (SPR) due to a high ratio of electron-surface collisions [4–7]. However, when immobilized on solid substrates, they become excellent SERS-active substrates since aggregation makes NPs arrange themselves within small sized gaps (1–2 nm) between neighboring NPs, that enhances the magnitude of the SERS effect [2,8].

Most of SERS substrates for the detection of potential organic pollutants [9–12], clinical samples [13,14], drugs [2,15,16], etc. reported in the literature are Au or Ag based. Despite the lower cost, Cu has been under used because of its inherent tendency to form a stable oxide layer [17]. Another factor is that the synthesis of Cu NPs is usually performed in organic media, which allows for better control over NP shape and size distribution [18], but may be disadvantageous for some applications. With the aims of broadening its application and to improve its stability, alloying copper with noble metals has become a general practice. Specifically, Au has been extensively used for this purpose because Cu and Au tend

* Corresponding author.
** Corresponding author.
E-mail addresses: gema.cabellocarramolino@abdn.ac.uk (G. Cabello), t.smith@abdn.ac.uk (T.A.D. Smith).

https://doi.org/10.1016/j.jallcom.2019.03.279
0925-8388/

to form stable phases when synthesized at high temperature [19–22]. Both metals have well-known plasmonic properties due to localized surface plasmon resonance (LSPR), which has significant importance in the development of SERS substrates. AuCu bimetallic NPs have been demonstrated to show enhanced LSPR depending on the Cu content that is associated with electromagnetic coupling effect [23–25]. On the other hand, the preparation of AuCu SERS substrates typically requires the use of templates and/or high temperatures, which make synthesis methods costly and, therefore, not suitable for scale up production. Some of these methods include laser ablation [26], porous anodic aluminum oxide template method [27], nanolithography (electron-beam lithography and focused ion beam milling) [28], impregnation/calcination [19], among many others that also require long reaction times, the use of harmful organic reagents and/or high-energy [23,29–31]. In such a way, the development of cost-effective preparation methods for highly active SERS substrates is a remaining goal in Raman scattering-based chemical sensing. Further, in the case of biological samples, some of the most commonly used techniques for detection, such as fluorescence microscopy, may induce misleading results as a consequence of photobleaching and/or sample contamination because of fluorescein labeling and phototoxicity.

Herein, we report an efficient, practical method for the synthesis of Cu@Au bimetallic nanoparticles, and their application as a versatile SERS substrate for the detection of several molecules of interest at the trace level. We have selected representative examples of compounds from different chemical families, which include sterols, herbicides, diamondoids cycloalkanes, pharmaceutical drugs and neurotransmitters and we have studied them under different wavelength excitation lines.

2. Materials and methods

2.1. Reagents and materials

All reagents (from Aldrich) were analytical grade and used as received. All solutions were prepared using demineralized and filtered water (18.2 MΩ cm) from an Elgastat water purification system (Elga, Bucks, UK).

2.2. Instrumentation

An Instrument for Microwave Accelerated Chemistry, model 521i from Resonance Instruments, Inc. was used for NPs synthesis, using 5 mL Wheaton reaction vials.

AF4-UV-ICPMS measurements were performed with an AF2000 MT FFF (Postnova Analytics, GmbH) and 8800 Triple Quadrupole ICP-MS/MS (Agilent, USA). UV/vis-detector at 525 nm; 20 μL injection volume; 2 mL min^{-1} cross flow, 0.5 mL min^{-1} detector flow, 3.6 mL min^{-1} (He); 1.18 L min^{-1} carrier gas (Ar) and spray chamber at 2 °C. Particle size was calculated by external calibration of UV–VIS elution times, using 5 nm, 15 nm, 50 nm and 60 nm Au NPs standards eluted in Milli-Q water. Particle size was reported as average diameter of triplicate measurements.

A JEM-1400 Plus transmission electron microscope (JEOL, Japan) operated at 120 kV was used for TEM images acquisition.

A PANalytical Empyrean Powder diffractometer operated at 30 kV was use for X-ray diffraction data acquisition (λ = 1.54059 Å, Cu Kα1 radiation, in θ–2θ mode at 0.01° s^{-1}).

UV/vis spectra were recorded with a Perkin Elmer spectrometer (LAMBDA 25), using 1 cm quartz cells.

XPS data were recorded under a pressure lower than 2×10^{-9} mbar with a PHOIBOS-150 hemispherical electron analyser equipped with nine channeltrons using Mg Kα radiation (1253.6 eV) and a constant pass energy of 20 eV. The X-ray source was operated at low power (100 W) to minimize radiation-induced changes on the samples. Repeated scans taken at different times along the Cu 2p, Au 4f and C 1s spectral regions indicated that the samples were stable under the X-ray beam and that the positions of the peaks were not affected by dynamic charge effects. The binding energy scale was referenced to the binding energy of the main C 1s signal which was set at 284.6 eV.

Raman spectra were collected with an inVia High Resolution Confocal Raman Spectrometer (Renishaw plc, Wotton-under-edge, UK), excitation line at 785 nm (8 mW maximum power) and 1200 lines/mm spectrographic grating. The excitation line at 514 nm was provided by an internal Ar ion laser (20 mW maximum power) and 2400 lines/mm spectrographic grating. A 50x objective for laser illumination and scattered light collection was used with a calculated laser focused spot diameter of 1.74 μm and 1.14 μm, respectively.

2.3. Synthesis of colloidal Cu@Au

CuAu NPs were synthesized by chemical reduction of the corresponding metallic salts using a mixture of ascorbic acid (AA) and trisodium citrate (TSC) under microwave-assisted heating (MW-h). A mixture of AA and TSC (1:2 M ratio) was vigorous stirred for 10 min. 500 μL of that solution were transferred to a MW vessel and 200 μL of $HAuCl_4 \cdot 3H_2O$ and $CuSO_4 \cdot 6H_2O$ (1:5 M ratio) were added and heated at 70 °C for 30 s (125 mA and 80 W magnetron output power). A reddish sol was obtained, which was twice centrifuged at 20 G's for 15 min and washed with deionized water. Au NPs and Cu NPs were synthesized following the same procedure but replacing the copper and the gold salt solution, respectively, for the corresponding volume of water. All samples were store at 4 °C until further use.

3. Results and discussion

3.1. Physical, chemical and morphological characterization

3.1.1. TEM

Fig. 1 shows the low-resolution TEM images of the NPs and the results of the average size are summarized in Table 1. Synthesis of Au, Cu and CuAu NPs was carried out under MW-h (panels up) and under conventional heating (panels down), for comparison. In all cases, NPs synthesized under MW-h were smaller in size than those synthesized by conventional heating. Improved size and shape distribution was obtained under MW-h, which has been already reported elsewhere [32] and associated with MW specific thermal effects that allow for better control over particle size distribution, shape and reaction yield [32–36]. Spherical Au NPs had diameters in the range of 10 nm–20 nm, whilst Cu NPs showed quasi-regular polyhedral shape with narrow size distribution of 150 nm. The as-synthesized CuAu NPs sols contained spherical particles of about 5 nm diameter. Reduced NP size with increasing Cu content has been reported elsewhere and related to a positive deviation of Vegard's Law for Au-rich solid solutions [37,38]. On the other hand, NPs synthesized under conventional heating (panels down) showed larger size and random shape distribution, which emphasizes the significance of the synthesis temperature on the morphological and structural parameters of the NPs.

3.1.2. AF4-UV-ICPMS

Fig. 2 shows the AF4 fractograms of the as-synthesized CuAu NPs (Fig. 2A) and Au NPs (Fig. 2B), which were stabilized with a PEG-SH shell to prevent aggregation (5.6 ± 0.3 nm thick) [39]. According to Eq. (1), the UV/vis detector allowed for NPs hydrodynamic size quantification based on the strong dependence of UV

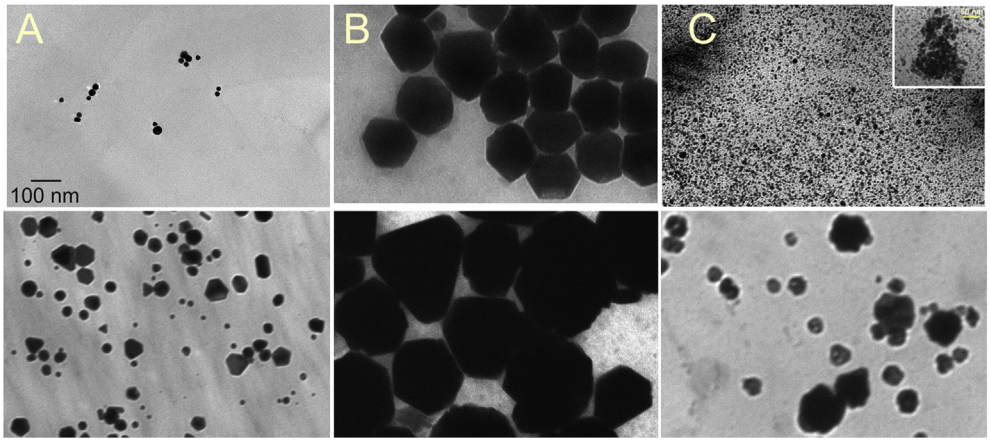

Fig. 1. TEM images of Au (A); Cu (B) and CuAu (C) NPs synthesized by microwave-assisted heating (panels up), and by conventional heating (panels down).

Table 1
Average diameter of NPs calculated from Fig. 1.

	Au	Cu	CuAu
MW	10–20 nm	150 nm	5 nm
No MW	15–75 nm	500 nm - 1 μm	10–70 nm

absorption of plasmonic particles with size [40–42]. The same calibration curve of Au standards reported elsewhere was used for the calculation of retention time [39]. Further, online coupling of the asymmetric flow field flow fractionation (AF4) coupled UV/vis system and ICPMS provided additional, specific multi-element detection and the capability to distinguish metal NPs from artefacts [43].

$$d_H = \left(\frac{2KTA}{\pi \cap V_c w t^0}\right) t_r \quad (1)$$

where d_H is the particle hydrodynamic diameter; K is the Boltzmann constant; T is the absolute temperature; A is the area of the accumulation wall; $\cap$ is the viscosity of the mobile phase; V_c is the cross flow rate; w is the channel width and t^0 and t_r are the void and retention time, respectively [44].

Concomitant bands at m/z 197 (Au, black line)) and m/z 63 (Cu, grey line)) eluting at 13 min in Fig. 2A, demonstrate the formation of self-assembled NPs with core diameter of 4.7 nm (±0.3 nm). The fractogram of Au NPs (Fig. 2B) showed a single band at 16.5 min, which corresponds to Au (m/z 197) with a core diameter of 12.7 nm (±0.3 nm). The larger diameter of the Au NPs compared with corresponding CuAu NPs, is in good agreement with results from TEM (Fig. 1C). Considering that the synthesis protocol was the same in both cases, it is clearly evidenced that combining Au with Cu lead to decreased NP size [38].

3.1.3. XPS

Cu and Au are well-known to form solid solutions over the whole range of compositions in bulk [45] in which, from a catalytic point of view, Au tends to act simply as an inert dilutant [46]. On the other hand, microstructural composition and surface distribution are of great importance considering optical properties, such as plasmonic effects.

Fig. 3A shows the wide scan X-ray photoelectron spectrum recorded from the as-synthesized CuAu nanoparticles. The spectrum is dominated by very intense C, O and Na signals, associated with a large amount of TSC still present in the sample. In fact, the C 1s spectrum (Fig. 3B) is a combination of the spectrum of sodium citrate and adventitious carbon [47]. This spectrum contains contributions at 284.6 eV, 286.1 eV, 287.7 eV and 288.8 eV. The first peak at 284.6 eV corresponds to C–C and C–H bonds (adventitious carbon is also responsible for this). The peak at 286.1 eV is associated with C–OH and/or CH_2 groups and the last one, at 288.2 eV, contains contributions from both COO–Na and COO(H) [47]. The

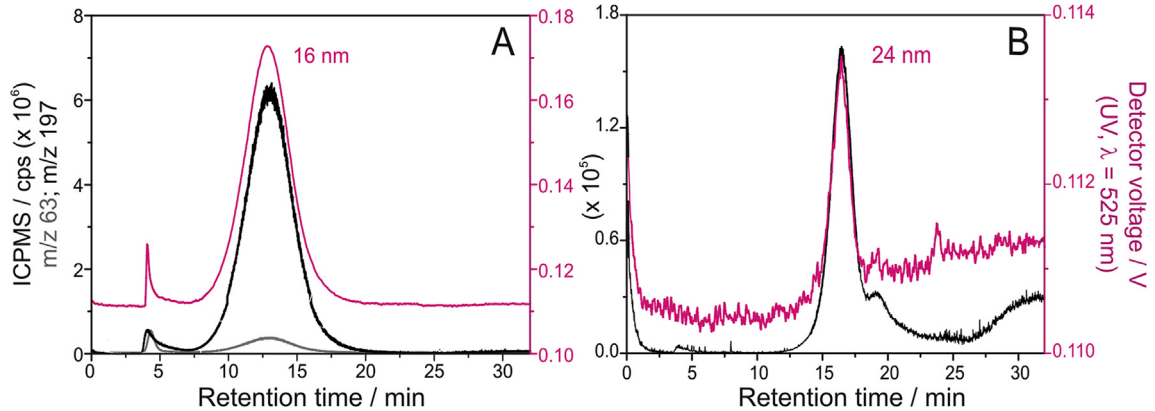

Fig. 2. AF4-UV-ICPMS fractograms of CuAu NPs (A) and Au NPs (B), all synthesized under MW-assisted heating. ICPMS: m/z 63 Cu (grey); m/z 197 Au (black). UV, λ = 525 nm (pink). (For interpretation of the references to colour in this figure legend, the reader is referred to the Web version of this article.)

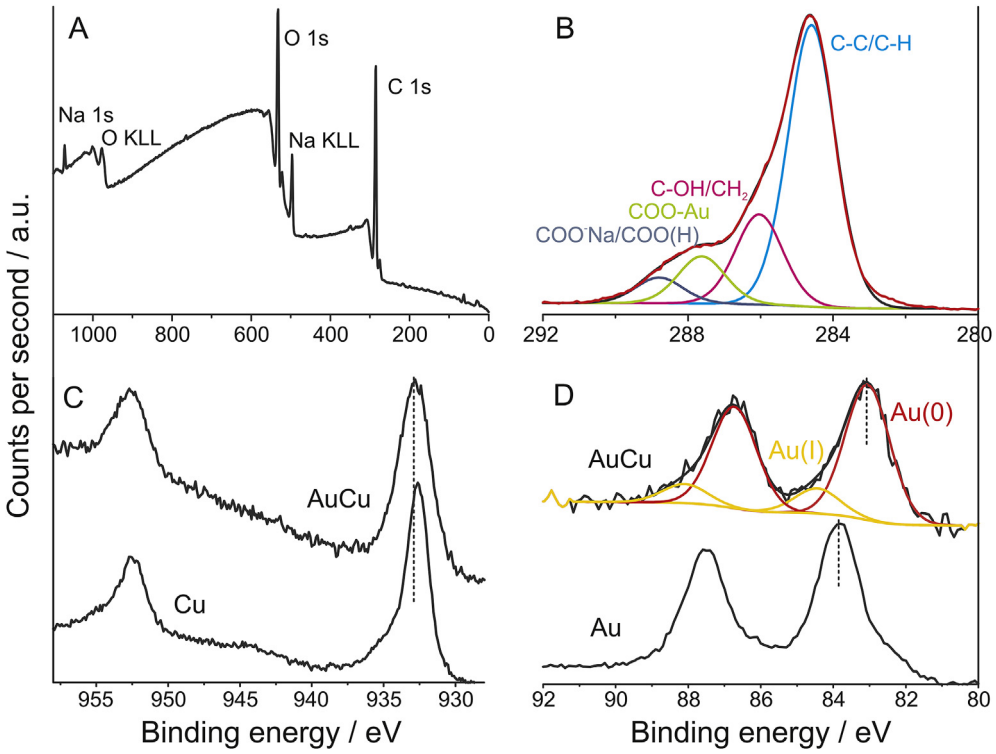

Fig. 3. X-ray photoelectron spectra. CuAu NPs, wide scan (A); C 1s (B); CuAu NPs and: Cu 2p (C); Au 4f (D).

third peak at 287.7 eV has been associated with COO–Au bonds and arises from the bonding of the citrate species with the gold surface [47]. This coordinated carboxylate species COO–Au appears to be of prime importance in stabilizing metal nanoparticles. Inspection of the spectrum depicted in Fig. 3A clearly shows the extremely weak intensity of the Cu 2p (925 eV - 960 eV region) and Au 4f (80 eV - 90 eV region) contributions which are hardly observed because of the large C, O and Na signals. This makes the precise quantification of copper and gold quite difficult, particularly taking into account the large difference in kinetic energy of the Au 4f and Cu 2p electrons whose intensities are attenuated very differently by the organic layer present on the samples.

Fig. 3C and D shows the Cu 2p and Au 4f X-ray photoelectron spectra recorded from CuAu NPs, respectively. The Cu 2p spectrum (Fig. 3C) is composed of a narrow spin-orbit doublet with binding energies of the Cu $2p_{3/2}$ and Cu $2p_{1/2}$ core levels of 932.8 eV and 952.4 eV, respectively. These values are within the range of those observed recently in citrate-stabilized core/shell Cu@Au nanoparticles and are compatible with copper in zero-valent state [48]. The spectral peaks are quite symmetrical. The absence of signals in the high binding energy side of the Cu 2p spin-orbit doublet and, more importantly, the lack of satellite structure in the region 940 eV - 946 eV rule out the presence of any Cu(II) component in the NPs [49].

The Au 4f spectrum (Fig. 3D) consists also of a spin-orbit doublet, which has been deconvoluted into two different doublets. The most intense one, having binding energies of the Au $4f_{7/2}$ and Au $4f_{5/2}$ core levels at 83.1 eV and 86.8 eV, respectively, is representative of zero-valent gold [48]. The second minor doublet (BE Au $4f_{7/2} = 84.5$ eV; BE Au $4f_{5/2} = 88.2$ eV) is associated with the coordinated carboxylate COO–Au species [47].

It is interesting to compare these binding energy values with those shown by single copper and gold nanoparticles. Fig. 3C and D shows the Cu 2p and Au 4f X-ray photoelectron spectra recorded from pure Cu and Au NPs, respectively. In the case of the spectrum from pure Cu NPs (Fig. 3C), the Cu 2p spectral lines are shifted by *ca.* +0.2 eV with respect to those observed in the CuAu NPs. Conversely, the binding energy values of the 4f lines in the Au 4f spectrum from pure Au NPS, spectral lines are shifted by *ca.* −0.7 eV with respect to those measured in CuAu NPs. A similar effect has been observed in CuAu NPs prepared by ammonia-evaporation-deposition-precipitation, which has been associated with the formation of a CuAu alloy [50]. The formation of an alloy, however, can be questionable in view of these shifts since, in general, it has been claimed that the binding energy of the Au 4f (Cu 2p) lines are shifted to higher (lower) binding energies when the concentration of Cu in the CuAu alloy increases (decreases) [51–53]. Although the shifts reported here, and those collected in Ref. [50], go in the opposite direction than would be expected in the case of the formation of an alloy, it is clear that they indicate the occurrence of electron transfer between Cu and Au. Particularly, since the shift in the Au 4f (Cu 2p) spectrum is negative (positive), indicating that the electron density on the gold (copper) atoms increases (decreases), results would be consistent with the occurrence of electron transfer from Cu to Au.

In view of the above results, which have shown the presence of large contribution from TSC, the absence of oxidized Cu species and the presence of both, zero-valent Au and COO–Au bonds, we can envisage a model for the CuAu NPs, which could consist in a core/shell structure, *i.e.*, a Cu metal core surrounded by a Au layer to which sodium citrate is bonded through the formation of carboxylate COO–Au species. This would explain the absence of oxidized copper species since the Cu core would be protected by the outer Au shell. Note that in the case of the single Cu NPs, where the outer Au layer does not exist, the asymmetry of the spectral lines in their high binding energy side and the occurrence of satellite peaks *ca.* 944.0 eV in the Cu 2p spectrum suggests the presence of a small Cu(II) contribution indicating that Cu NPs are slightly oxidized at

the surface. The proposed core/shell structure would also explain why XPS results are not exactly compatible with the formation of a CuAu alloy.

3.1.4. UV/vis, XRD & SEM

SPR bands of the as-synthesized NPs (PEG-SH coated) were followed by UV/vis spectroscopy (Fig. 4A). Au showed a band with absorption maximum at 521 nm, which is characteristic of <20 nm diameter NPs [54]. A broad band at 624 nm was associated with the quenching of SPR by large Cu NPs [33]. The band at 270 nm has been previously reported for Cu(0) NPs [55], which supports the results obtained by XPS related to the occurrence of core-shell NPs, as discussed above. Consequently, the SPR band at 568 nm was assigned to Cu@Au NPs, based on (i) the red-shift of the SPR band despite the smaller size of the NPs (also considering that the size of the NPs decreased with higher Cu content) and (ii) the broadening of the band, which has been ascribed to larger interband contributions of Cu compared to Au [56].

Fig. 4B shows the XRD patterns of the CuAu films deposited on plain microscope glass slides. Au peaks are clearly shifted to higher Bragg's angle values, which evidences decreased distance between Au atoms. Cu@Au particles (blue) showed main diffraction peaks at $2\theta = 38.7°$, 44.9°, 65.2°, 78.1° and 82.2°. All peaks were slightly shifted to higher diffraction angles, compared to those of synthesized pure Au and the corresponding Au pattern, as a result of Au lattice compression. Diffraction angles were assigned to (111), (200), (220), (311) and (222) planes, respectively, of *Pm*-3m $Au_{0.8}Cu_{0.2}$ (#72-5241, primitive cubic structure).

Random CuAu films were deposited on glass slide substrates and the surface morphology was described by SEM (Fig. 4C). The surface displayed a thick-porous layer as a result of high-coverage of coalesced globular AuCu particles and their aggregates.

The composition of the SERS substrate was also characterized by EDX, by acquiring several spectra from SEM micrograph in Fig. 4D. All results corroborated the presence of both, Au and Cu on the substrate.

3.2. Raman scattering: RhB and MB. scattering signal enhancement factor

The performance of CuAu SERS substrates for chemical sensing was first evaluated using two probe molecules: rhodamine B (RhB) and methylene blue (MB), both 10^{-4} M, under 785 nm and 514 nm excitation line, respectively (Fig. 5). Different laser sources were selected strictly based on the target analyte: 785 nm for RhB, which shows native fluorescence in the visible, and 514 nm for MB, which is considered a general purpose excitation line that is blue-shifted with respect to the maximum of the LSPR leading to a significant signal enhancement because of the formation of hot spots [57].

Fig. 5A shows the Raman spectra of RhB on a naked-Si wafer, and on Au, Cu and Cu@Au films on a Si wafer (a-d, respectively), collected under an excitation source emitting at 785 nm. Negligible Raman signal was obtained from naked Si, Au and Cu substrates (Fig. 5A a, b and c, respectively). On the other hand, typical bands associated with RhB appeared on the spectrum obtained from CuAu substrates (Fig. 5A d). Main bands were ascribed to xanthene ring bending, at 619 cm^{-1}; methyl rocking, at 1077 cm^{-1}; $\delta_{C\text{-}H}$ at 1196 cm^{-1}; methyl wagging, at 1282 cm^{-1} and xanthene ring stretching, at 1361 cm^{-1}, 1510 cm^{-1}, 1533 cm^{-1} and 1647 cm^{-1}.

Spectra of MB on the same substrates are shown in Fig. 5B, but acquired using a laser source emitting at 514 nm. In this case, Au and Cu substrates (Fig. 5B b and c, respectively) showed a weak band at 1625 cm^{-1}, associated with the characteristic $\nu_{C\text{-}C}$(ring) of MB. More intense bands were obtained from CuAu substrates

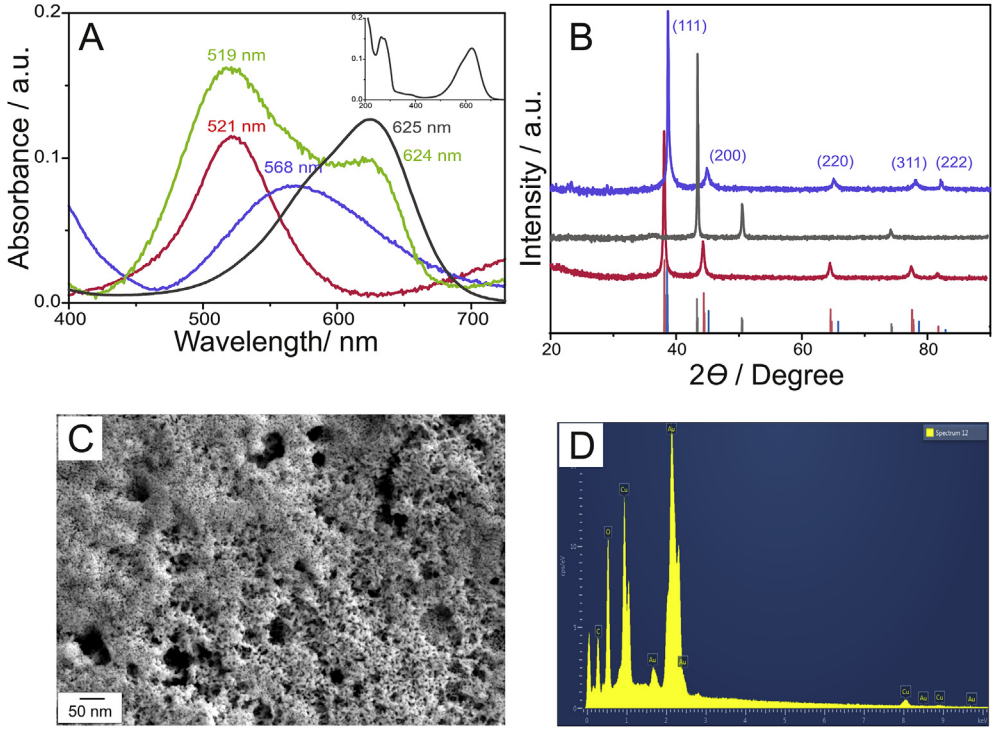

Fig. 4. (A) UV/vis spectra of Au (red line); Cu (grey line and inset); CuAu (blue line) and Au + Cu (synthesized separately, green line) nanoparticles, all synthesized under MW-assisted heating. (B) XRD characterization of as-prepared Cu@Au films deposited on glass slide (blue). Monometallic as-synthesized Cu and Au (grey and red, respectively) and their corresponding patterns ((#4-836, light grey and #4-784, light red). (C) Top view SEM images of as-synthesized CuAu NPs dried on a Si wafer substrate. (D) EDX screening of sample in Fig. 4C. (For interpretation of the references to colour in this figure legend, the reader is referred to the Web version of this article.)

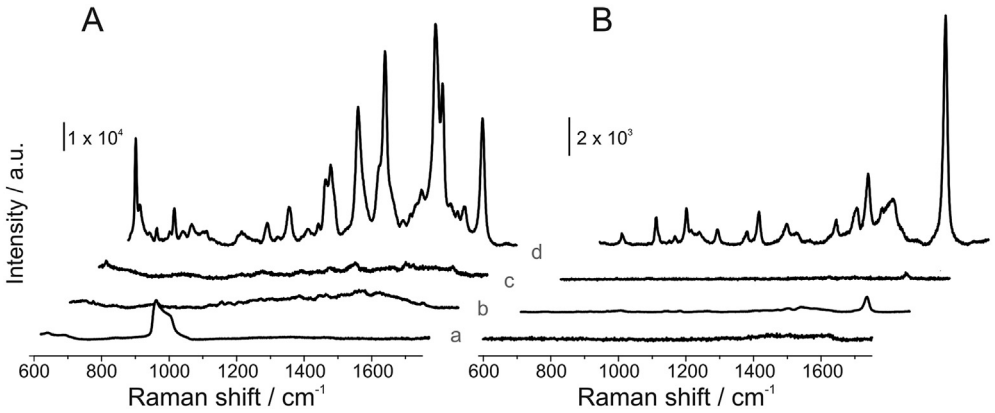

Fig. 5. SERS spectra of (A) RhB and (B) MB, both 10^{-4} M/EtOH on naked Si wafer (a) and Si covered by as-synthesized Au (b), Cu (c) and (d) Cu@Au NPs.

(Fig. 5B d), *i.e.*, skeletal deformation of C–N–C, at 445 cm^{-1} and 497 cm^{-1}; skeletal deformation of C–S–C, at 593 cm^{-1}; out-of-plane $\delta_{C\text{-}H}$, at 665 cm^{-1}; in-plane $\delta_{C\text{-}H}$ bands between 770 cm^{-1} and 1153 cm^{-1}; $\nu_{C\text{-}N}$, at 1182 cm^{-1}; in-plane ring $\delta_{C\text{-}H}$, at 1300 cm^{-1}; symmetric $\nu_{C\text{-}N}$, at 1393 cm^{-1}; asymmetric $\nu_{C\text{-}N}$, at 1436 cm^{-1} and 1471 cm^{-1} and ring $\nu_{C\text{-}C}$, at 1625 cm^{-1}.

These results demonstrate to the versatility of our SERS-active substrates for several laser excitation lines, compared to typical Au substrates. Besides its inherent high stability, Au has been extensively reported to show enhanced SERS effect compared to Cu, although it can only be efficiently excited with red laser light. Interestingly, in our case, enhanced electromagnetic effect has been found under two different excitation lines, compared to both Au and Cu substrate that led to a detection limit of 10^{-12} M and 10^{-9} M for RhB and MB, respectively.

The SERS average enhancement factor (EF) was calculated following the band of RhB at 1647 cm^{-1} (785 nm excitation line) by the equation:

$$EF = \frac{I_{SERS}}{I_0} \times \frac{C_0}{C_{SERS}} \quad (2)$$

where I_{SERS} and I_o are the band intensity of the SERS and the naked substrate, respectively, and C_{SERS} and C_o are the concentration of RhB solution in EtOH on the Cu@Au substrate and the Si wafer (10^{-4} M and 10^{-2} M, respectively).

The calculated EF was of the order of 3×10^5, which is in good agreement with reproducible/˜realistic' EFs, which typical values lie in the range from 10^4 to 10^7 [28]. It is worth mentioning that several aspects need to be consider when comparing SERS substrates, such as reproducibility, cost-effective preparation, reliability, etc., that are more difficult to quantify.

3.3. SERS chemical sensing

To demonstrate the versatility of our CuAu NPs as SERS-active substrates, some characteristic samples from different chemical families of interest were studied, under 785 nm and 514 nm wavelength excitation lines, and the results are shown in Fig. 6.

3.3.1. Cholesterol

The development of fast, cost-effective and highly sensitive sensors is of great interest for biomedical applications. Cholesterol may be considered as a reference in this field, since high levels in blood (>μM) [58] may be related to cardiovascular diseases. Raman spectroscopy has been successfully applied for the detection of cholesterol in pathologic samples [59] and, most recently, in cells using architectured SERS substrates [60,61].

AuCu NPs were used as SERS substrates to collect spectra of cholesterol (10^{-8} M) under excitation line of 514 nm (Fig. 6A, green line). Pure cholesterol (black line) spectrum was also acquired for comparison. Two distinctive bands at 605 cm^{-1} and 700 cm^{-1} were assigned to the vibrational modes of the sterol ring (C–C backbone vibration). These bands unequivocally demonstrate the presence of cholesterol on the SERS substrate. Other bands, appeared at 1440 cm^{-1}, $\delta_{C\text{-}H}$ of lipids (the absence of a band at 1746 cm^{-1} indicates that the lipid is not a triglyceride); at 1467 cm^{-1}, assigned to CH_2/CH_3 scissoring and that at 1670 cm^{-1}, ascribed to the $\nu_{C=C}$ of the steroid nucleus. Bands at higher frequency, 2864 cm^{-1} and 2930 cm^{-1} are typically associated with ν_s CH_2 and CH_3, respectively [59].

3.3.2. Propanil

3,4-dichloropropionanilide (propanil) is a worldwide used herbicide. Its detection at the trace level is important from an environmental point of view because its potential pollutant activity, usually associated with its degradation products as a consequence of photochemical reactions. Detection of propanil has been typically carried out by classical conventional analytical methods, such as UV/vis and fluorescence spectroscopy, liquid chromatography, mass spectrometry, etc., at concentrations up to 10^{-8} M [62–64].

Raman spectra of propanil on CuAu substrates are shown in Fig. 6B (10^{-8} M propanil, red line and pure propanil, clack line). Bands at 1235 cm^{-1}, ascribed to $\nu_{Ph\text{-}NH}$, and those at 1298 cm^{-1} and 1530 cm^{-1}, associated with N–H waging, unequivocally allowed for the determination of propanil. Other bands were ascribed to whole skeleton stretching (590 cm^{-1} and 875 cm^{-1}); out-of-plane ring $\delta_{C\text{-}H}$ (901 cm^{-1} and 935 cm^{-1}); ring triangle bending (1029 cm^{-1}); in-plane ring $\delta_{C\text{-}C\text{-}H}$ and ring breathing (1128 cm^{-1}); bands at 1298 cm^{-1} and 1530 cm^{-1} also have contributions from both, ring $\nu_{C=C}$ and in-plane CH_2 rocking and from ring $\nu_{C=C}$, respectively. The band at higher frequencies was ascribed again to ring $\nu_{C=C}$.

3.3.3. Adamantane

Diamond hydrocarbons derived from petroleum have gained great interest because of their unusual cage-structured properties [65]. Adamantane was discovered in 1933 and it can be considered the primitive cell of a complex family of the so-called plastic crystals. Relatively recently it has found a role in the development of chemical sensors based on supramolecular polymeric materials [66,67]. Specifically, adamantane has been used in the construction of host-guest systems because of its high affinity for macrocyclic complexes, such as cyclodextrins [68]. Consequently, detection of

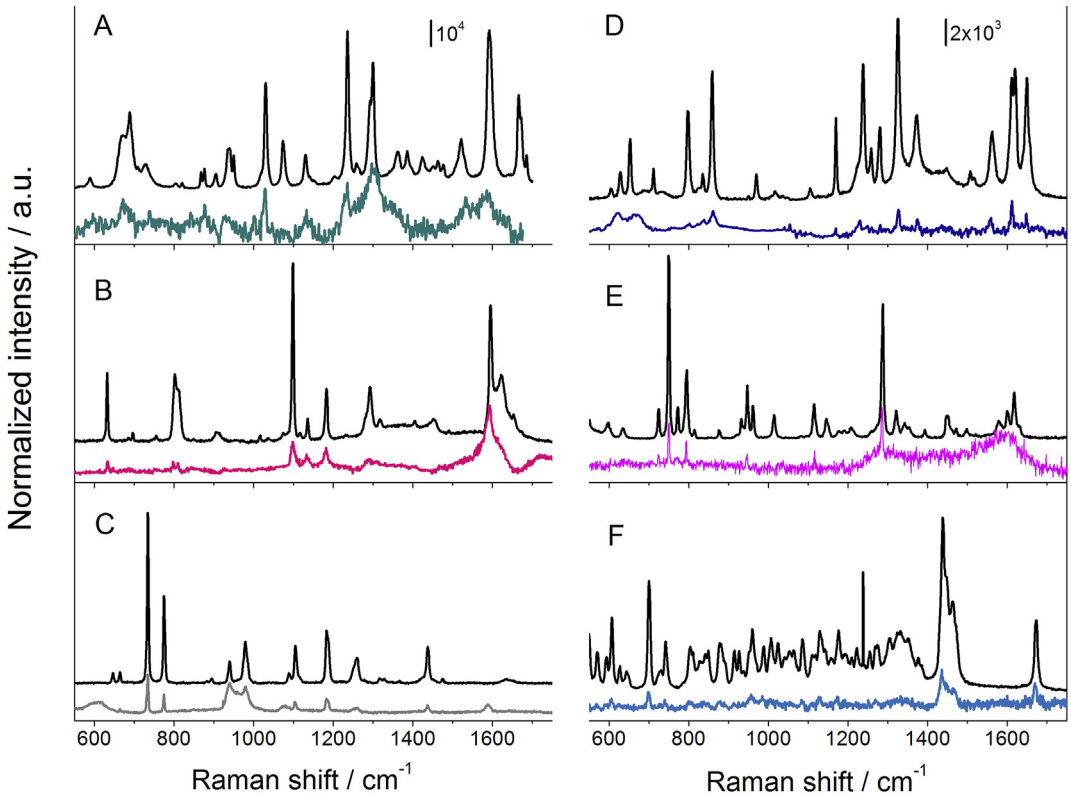

Fig. 6. Raman and SERS spectra of (A) cholesterol; (B) propanil; (C) adamantane; (D) AMP; (E) MBA and (F) dopamine, carried out under excitation line of 785 nm (left panels) and 514 nm (right panels).

adamantane is necessary for a detailed characterization of the sensor surface labelling. Fig. 6C shows the Raman spectra of pure adamantane (black) and 10^{-8} M adamantane (grey) on CuAu SERS substrates, both collected under an excitation line of 785 nm. Main characteristic bands of adamantane can be clearly appreciate despite of the low concentration, such as $\nu_{C\text{-}C}$ breathing (bands at 735 cm^{-1}, 775 cm^{-1} and 940 cm^{-1}); $\delta_{C\text{-}C\text{-}C}$ at 978 cm^{-1}; $\delta_{H\text{-}C\text{-}C}$ at 1104 cm^{-1} and $\delta_{H\text{-}C\text{-}H}$ at 1436 cm^{-1}.

3.3.4. Acetaminophen (AMP)

Effective and reliable detection of pharmaceutical drugs is a remaining goal in Analytical Chemistry because of their potential environmental impact. Acetaminophen is an extensively used pharmaceutical, which cannot be efficiently removed from treated waste water and, therefore, tends to reach agricultural activity even at the ppm level [69]. Acetaminophen detection has been carried out using several different techniques, including electrochemical methods, infrared spectroscopy, chromatography and electrophoresis, among many others [70–74], which are certainly complex and highly-time consuming.

Fig. 6D shows the Raman spectra of pure acetaminophen (black) and 10^{-8} M acetaminophen (blue) on CuAu SERS substrates, both collected under excitation line of 785 nm. Detection of acetaminophen was demonstrated by the presence of bands associated with the amide group, such as $\nu_{C\text{-}N}$ at 1233 cm^{-1}, O–H and C–O combination, (ar)-$\nu_{C\text{-}N}$ at 1279 cm^{-1}, $\nu_{\text{-}H\text{-}N\text{-}C=O}$ at 1558 cm^{-1}, $\delta_{N\text{-}H}$ at 1611 cm^{-1} and $\nu_{C\text{-}O}$ at 1649 cm^{-1}. Other bands were identified as $\nu_{C\text{-}C,\ Ph}$ at 800 cm^{-1}, out-of-plane $\delta_{C\text{-}H,\ Ph}$ at 839 cm^{-1}, $\nu_{C\text{-}H,\ Ph}$ (breathing) at 860 cm^{-1}, in-plane $\delta_{C\text{-}H,\ Ph}$ at 1170 cm^{-1}, $\delta_{C\text{-}H}$ at 1324 cm^{-1} and, $\delta_{s\ CH3}$ (umbrella) at 1373 cm^{-1}.

3.3.5. 4-Mercaptobenzoic acid (MBA)

Despite 4-mercaptobenzoic acid has been extensively used as Raman probe molecule, there is a remaining interest in the study of adsorption binding sites, which may also be related to the formation of self-assembled monolayers (SAMs) on electrodes and for applications in nanotechnology. Raman spectra of 10^{-8} M MBA and solid MBA on CuAu substrates are shown in Fig. 6E (pink line and black line, respectively). Bands at 632 cm^{-1}, 799 cm^{-1}, 1098 cm^{-1} and 1594 cm^{-1} were assigned to aromatic ring vibrations and those at 1135 cm^{-1} and 1180 cm^{-1}, both to δ_{CH}. Bands at 810 cm^{-1} and at 1612 cm^{-1} (weak), were associated with ω_{COO^-} and $\nu_{s\ COO^-}$, respectively, which specifically indicate dimerization of the carboxylic group. Further, the absence of a band associated with δ_{SH} at 915 cm^{-1}, suggests dissociation of S–H bond, as previously reported to occur on metal surfaces [75,76].

3.3.6. Dopamine

Dopamine detection is of biological interest because of its association with neurological disorders. It is found in the synaptic cleft between adjacent neuron cells [1]. Raman scattering has arisen as a powerful tool for detecting changes in dopamine bonds associated with the interaction with pharmaceutical drugs.

Fig. 6F shows the Raman spectra of pure dopamine (black line) and 10^{-8} M dopamine (cyan line) on CuAu SERS substrates. Bands at 750 cm^{-1}, associated with out-of-plane δ_{CH} and ring bending; at 795 cm^{-1} were associated with in-plane δ_{CH} and ring bending, associated with NH twisting, CH wagging and ring bending, at 950 cm^{-1}; CH twisting, NH twisting and ν_{CN}, at 1116 cm^{-1} and ring breathing, CH aromatic rocking and CH twisting modes, at 1285 cm^{-1}. The detection of dopamine is demonstrated for the occurrence of bands associated with the amine group.

4. Conclusions

This work describes a new approach for the synthesis of Cu@Au self-assembled nanoparticles and their application as versatile SERS substrates for chemical sensing, which includes biomolecules.

The synthesis was carried out using a mixture of reducing agents under MW-assisted heating.

NP size (4.7 nm diameter) was determined by AF4-UV-vis and confirmed by TEM.

XRD, XPS and UV/vis spectroscopy showed the occurrence of bimetallic NPs and, specifically, XPS demonstrated the absence of both, copper oxide and alloy formation but the occurrence of electron transfer from copper to gold. Based on these findings we assume NPs to arrange themselves in a core/shell configuration in which the gold shell prevents for copper oxidation that also validates the non-occurrence of alloy formation.

CuAu NPs were deposited on naked Si wafers, which allowed for NPs to arrange themselves within small sized gaps between neighboring NPs (1–2 nm). In such a way, SERS substrates based on Cu@Au NPs showed larger calculated SERS enhancement factor (3×10^5), compared to their monometallic counterparts, which was ascribed to enhanced electromagnetic effect, *i.e.*, electromagnetic coupling of self-assembled bimetallic NPs.

The prepared substrates were used for the detection of different molecules of interest, representative of a vast family of compounds at the trace level, including biomolecules and potential water pollutants. Measurements were carried out under two different excitation lines, *i.e.*, 514 nm and 785 nm, which further confirms the versatility of these SERS-active substrates.

Au NPs have been extensively used for this purpose, but bimetallic substrates, like the one described here, to the best of our knowledge have not been previously reported or are scarce.

Based on the high sensitivity provided by bimetallic CuAu SERS substrates in combination with cost-effective preparation, it is suggested that our as-prepared Cu@Au NPs may ensue as an efficient tool for scale up detection of a wide range of analytes of interest.

Acknowledgments

Funded by Chief Scientists Office (TCS/16/07), Tenovus Scotland (G15-03) and the University of Aberdeen Development Trust. KCN gratefully acknowledges the University of Aberdeen for the Elphinstone PhD scholarship (RG13451-10) and to Postnova Analytics UK for the loan of the AF4 system together with training, support, and advice on the technique. AM Mendez gratefully acknowledges CONICYT (National Commission of Scientific and Technological Research, Chile) for scholarship (21160174). Microscopy was performed in the Microscopy and Histology Core Facility at the University of Aberdeen. GC gratefully acknowledges the advice of Dr Shuiyu Lu (NIH, Maryland) in relation to the use of the MW reactor and Dr R.A Davoglio for useful discussion and suggestions.

References

[1] A.P. Silwal, R. Yadav, J.E. Sprague, H.P. Lu, Raman spectroscopic signature markers of dopamine–human dopamine transporter interaction in living cells, ACS Chem. Neurosci. 8 (2017) 1510–1518.
[2] P. Mosier-Boss, Review of SERS substrates for chemical sensing, Nanomaterials 7 (2017) 142.
[3] V. Garg, B.S. Sengar, V. Awasthi, Aaryashree, P. Sharma, C. Mukherjee, S. Kumar, S. Mukherjee, Localized surface plasmon resonance on Au nanoparticles: tuning and exploitation for performance enhancement in ultrathin photovoltaics, RSC Adv. 6 (2016) 26216–26226.
[4] U. Kreibig, Kramers Kronig analysis of the optical properties of small silver particles, Z. Angew. Phys. 234 (1970) 307–318.
[5] U. Kreibig, C.v. Fragstein, The limitation of electron mean free path in small silver particles, Z. Angew. Phys. 224 (1969) 307–323.
[6] X. Huang, M.A. El-Sayed, Gold nanoparticles: optical properties and implementations in cancer diagnosis and photothermal therapy, J. Adv. Res. 1 (2010) 13–28.
[7] S. Link, M.A. El-Sayed, Size and temperature dependence of the plasmon absorption of colloidal gold nanoparticles, J. Phys. Chem. B 103 (1999) 4212–4217.
[8] S.J. Oldenburg, R.D. Averitt, S.L. Westcott, N.J. Halas, Nanoengineering of optical resonances, Chem. Phys. Lett. 288 (1998) 243–247.
[9] M. Leona, J. Stenger, E. Ferloni, Application of surface-enhanced Raman scattering techniques to the ultrasensitive identification of natural dyes in works of art, J. Raman Spectrosc. 37 (2006) 981–992.
[10] K. Pei, M. Su, L. Chen, X. Zheng, Excited-state structural dynamics of propanil in the S2 state: resonance Raman and first-principle investigation, J. Phys. Chem. B 116 (2012) 7914–7919.
[11] J.B. Jackson, N.J. Halas, Surface-enhanced Raman scattering on tunable plasmonic nanoparticle substrates, Proc. Natl. Acad. Sci. 101 (2004) 17930.
[12] B. Sharma, R.R. Frontiera, A.-I. Henry, E. Ringe, R.P. Van Duyne, SERS: materials, applications, and the future, Mater. Today 15 (2012) 16–25.
[13] A.S. Moody, B. Sharma, Multi-metal, multi-wavelength surface-enhanced Raman spectroscopy detection of neurotransmitters, ACS Chem. Neurosci. 9 (2018) 1380–1387.
[14] B.K. Jena, B.K. Mishra, S. Bohidar, Synthesis of branched Ag nanoflowers based on a bioinspired technique: their surface enhanced Raman scattering and antibacterial activity, J. Phys. Chem. C 113 (2009) 14753–14758.
[15] X. Niu, X. Li, W. Chen, X. Li, W. Weng, C. Yin, R. Dong, W. Sun, G. Li, Three-dimensional reduced graphene oxide aerogel modified electrode for the sensitive quercetin sensing and its application, Mater. Sci. Eng. C 89 (2018) 230–236.
[16] M. Paczkowska, K. Lewandowska, W. Bednarski, M. Mizera, A. Podborska, A. Krause, J. Cielecka-Piontek, Application of spectroscopic methods for identification (FT-IR, Raman spectroscopy) and determination (UV, EPR) of quercetin-3-O-rutinoside. Experimental and DFT based approach, Spectrochim. Acta, Part A 140 (2015) 132–139.
[17] T. Ramani, K. Leon Prasanth, B. Sreedhar, Air stable colloidal copper nanoparticles: synthesis, characterization and their surface-enhanced Raman scattering properties, Phys. E 77 (2016) 65–71.
[18] A. Sarkar, T. Mukherjee, S. Kapoor, PVP-stabilized copper Nanoparticles: a reusable catalyst for “click” reaction between terminal alkynes and azides in nonaqueous solvents, J. Phys. Chem. C 112 (2008) 3334–3340.
[19] C.L. Bracey, P.R. Ellis, G.J. Hutchings, Application of copper–gold alloys in catalysis: current status and future perspectives, Chem. Soc. Rev. 38 (2009) 2231–2243.
[20] L. Vegard, H. Dale, An investigation of mixed crystals and alloys, Z. Kristallogr. 67 (1928) 148–161.
[21] A.E.V. Arkel, J. Basart., Atomic distances in mixed crystals of gold and copper, Z. Kristallogr. 68 475-476.
[22] C.S. Smith, Note on the crystal structure of copper-gold alloys, Min. Met. (1928) 458.
[23] Y. Gafner, S. Gafner, L. Redel, I. Zamulin, Dual structural transition in small nanoparticles of Cu-Au alloy, J. Nanoparticle Res. 20 (2018) 51.
[24] P. Srinoi, Y.-T. Chen, V. Vittur, D.M. Marquez, R.T. Lee, Bimetallic nanoparticles: enhanced magnetic and optical properties for emerging biological applications, Appl. Sci. 8 (2018).
[25] Y.E. Ejorh, W.H. Ilsley, B.G. Ooi, Elucidating the chemisorption phenomena in SERS studies via computational modeling, OPJ 8 (2018) 212–234.
[26] M. Sree Satya Bharati, C. Byram, V.R. Soma, Femtosecond laser fabricated Ag@Au and Cu@Au alloy nanoparticles for surface enhanced Raman spectroscopy based trace explosives detection, Front. Physiol. 6 (2018).
[27] K. Chen, X. Zhang, D.R. MacFarlane, Ultrasensitive surface-enhanced Raman scattering detection of urea by highly ordered Au/Cu hybrid nanostructure arrays, Chem. Commun. 53 (2017) 7949–7952.
[28] M. Fan, G.F.S. Andrade, A.G. Brolo, A review on the fabrication of substrates for surface enhanced Raman spectroscopy and their applications in analytical chemistry, Anal. Chim. Acta 693 (2011) 7–25.
[29] F. Burpo, E. Nagelli, L. Morris, K. Woronowicz, A. Mitropoulos, Salt-mediated Au-Cu nanofoam and Au-Cu-Pd porous macrobeam synthesis, Molecules 23 (2018) 1701.
[30] I. Barroso-Martín, E. Moretti, A. Talon, L. Storaro, E. Rodríguez-Castellón, A. Infantes-Molina, Au and AuCu nanoparticles supported on SBA-15 ordered mesoporous titania-silica as catalysts for methylene blue photodegradation, Materials 11 (2018) 890.
[31] E. Andrews, Y. Fang, J. Flake, Electrochemical reduction of CO2 at CuAu nanoparticles: size and alloy effects, J. Appl. Electrochem. 48 (2018) 435–441.
[32] G. Cabello, R.A. Davoglio, F.W. Hartl, J.F. Marco, E.C. Pereira, S.R. Biaggio, H. Varela, A. Cuesta, Microwave-assisted synthesis of Pt-Au nanoparticles with enhanced electrocatalytic activity for the oxidation of formic acid, Electrochim. Acta 224 (2017) 56–63.
[33] M. Blosi, S. Ortelli, A. Costa, M. Dondi, A. Lolli, S. Andreoli, P. Benito, S. Albonetti, Bimetallic nanoparticles as efficient catalysts: facile and green microwave synthesis, Materials 9 (2016) 550.
[34] S. Komarneni, D. Noh Young, Y. Kim Joo, H. Kim Seok, H. Katsuki, Solvothermal/hydrothermal synthesis of metal oxides and metal powders with and without microwaves, Z. Naturforsch. B Chem. Sci. (2010) 1033.

[35] A. de la Hoz, A. Diaz-Ortiz, A. Moreno, Microwaves in organic synthesis. Thermal and non-thermal microwave effects, Chem. Soc. Rev. 34 (2005) 164–178.
[36] B.I. Kharisov, O.V. Kharissova, U. Ortiz Méndez, Microwave hydrothermal and solvothermal processing of materials and compounds, in: W. Cao (Ed.), The Development and Application of Microwave Heating, 2012.
[37] D. König, K. Richter, A. Siegel, A.-V. Mudring, A. Ludwig, High-throughput fabrication of Au–Cu nanoparticle libraries by combinatorial sputtering in ionic liquids, Adv. Funct. Mater. 24 (2014) 2049–2056.
[38] M.A. Jaswon, W.G. Henry, G.V. Raynor, The cohesion of alloys: I. Intermetallic systems formed by copper, silver and gold, and deviations from vegard's Law, Proc. Phys. Soc. Lond. Sect. B 64 (1951) 177.
[39] G. Cabello, K. Nwoko, M. Mingarelli, A.C. McLaughlin, L. Trembleau, J. Feldmann, A. Cuesta, T.A.D. Smith, Physico-chemical tools: towards a detailed understanding of the architecture of targeted radiotherapy nanoparticles, ACS Appl. Bio Mater. 1 (5) (2018) 1639–1646.
[40] S.A. Cumberland, J.R. Lead, Particle size distributions of silver nanoparticles at environmentally relevant conditions, J. Chromatogr. A 1216 (2009) 9099–9105.
[41] L. Calzolai, D. Gilliland, C.P. Garcìa, F. Rossi, Separation and characterization of gold nanoparticle mixtures by flow-field-flow fractionation, J. Chromatogr. A 1218 (2011) 4234–4239.
[42] A.J. Bednar, A.R. Poda, D.M. Mitrano, A.J. Kennedy, E.P. Gray, J.F. Ranville, C.A. Hayes, F.H. Crocker, J.A. Steevens, Comparison of on-line detectors for field flow fractionation analysis of nanomaterials, Talanta 104 (2013) 140–148.
[43] B. Schmidt, K. Loeschner, N. Hadrup, A. Mortensen, J.J. Sloth, C. Bender Koch, E.H. Larsen, Quantitative characterization of gold nanoparticles by field-flow fractionation coupled online with light scattering detection and inductively coupled plasma mass spectrometry, Anal. Chem. 83 (2011) 2461–2468.
[44] H. Dou, E.C. Jung, S. Lee, Factors affecting measurement of channel thickness in asymmetrical flow field-flow fractionation, J. Chromatogr. A 1393 (2015) 115–121.
[45] Metal-Metal Bonds and Clusters in Chemistry and Catalysis, Springer US, New York, 1990.
[46] J. Schwank, Gold in bimetallic catalysts, Gold Bull. 18 (1985) 2–10.
[47] J.-W. Park, J.S. Shumaker-Parry, Structural study of citrate layers on gold nanoparticles: role of intermolecular interactions in stabilizing nanoparticles, JACS 136 (2014) 1907–1921.
[48] J. Zhang, X. Xu, C. Yang, F. Yang, X. Yang, Colorimetric iodide recognition and sensing by citrate-stabilized core/shell Cu@Au nanoparticles, Anal. Chem. 83 (2011) 3911–3917.
[49] S.J. Stewart, M. Multigner, J.F. Marco, F.J. Berry, A. Hernando, J.M. González, Thermal dependence of the magnetization of antiferromagnetic copper(II) oxide nanoparticles, Solid State Commun. 130 (2004) 247–251.
[50] A. Yin, C. Wen, W.-L. Dai, K. Fan, Nanocasting of CuAu alloy nanoparticles for methyl glycolate synthesis, J. Mater. Chem. 21 (2011) 8997–8999.
[51] P. Steiner, S. Hüfner, Thermochemical data of alloys from photoelectron spectroscopy, Acta Metall. 29 (1981) 1885–1898.
[52] M.-J. Kim, H.-J. Na, K.C. Lee, E.A. Yoo, M. Lee, Preparation and characterization of Au–Ag and Au–Cu alloy nanoparticles in chloroform, J. Mater. Chem. 13 (2003) 1789–1792.
[53] R.E. Schaak, A.K. Sra, B.M. Leonard, R.E. Cable, J.C. Bauer, Y.-F. Han, J. Means, W. Teizer, Y. Vasquez, E.S. Funck, Metallurgy in a Beaker: nanoparticle toolkit for the rapid low-temperature solution synthesis of functional multimetallic solid-state materials, JACS 127 (2005) 3506–3515.
[54] P.N. Njoki, I.I.S. Lim, D. Mott, H.-Y. Park, B. Khan, S. Mishra, R. Sujakumar, J. Luo, C.-J. Zhong, Size correlation of optical and spectroscopic properties for gold nanoparticles, J. Phys. Chem. C 111 (2007) 14664–14669.
[55] P. Christian, M. Bromfield, Preparation of small silver, gold and copper nanoparticles which disperse in both polar and non-polar solvents, J. Mater. Chem. 20 (2010) 1135–1139.
[56] N.E. Motl, E. Ewusi-Annan, I.T. Sines, L. Jensen, R.E. Schaak, Au–Cu alloy nanoparticles with tunable compositions and plasmonic properties: experimental determination of composition and correlation with theory, J. Phys. Chem. C 114 (2010) 19263–19269.
[57] R.A. Álvarez-Puebla, Effects of the excitation wavelength on the SERS spectrum, J. Phys. Chem. Lett. 3 (2012) 857–866.
[58] O. Guselnikova, Y. Kalachyova, K. Hrobonova, M. Trusova, J. Barek, P. Postnikov, V. Svorcik, O. Lyutakov, SERS platform for detection of lipids and disease markers prepared using modification of plasmonic-active gold gratings by lipophilic moieties, Sens. Actuators, B 265 (2018) 182–192.
[59] J.J. Baraga, M.S. Feld, R.P. Rava, In situ optical histochemistry of human artery using near infrared Fourier transform Raman spectroscopy, PNAS 89 (1992) 3473–3477.
[60] J. Genova, M. Petrov, I. Bivas, P. Rafailov, H. Naradikian, B. Katranchev, Fourier-transform infrared and Raman characterization of bilayer membranes of the phospholipid SOPC and its mixtures with cholesterol, Colloids Surf., A 557 (2018) 85–93.
[61] S.S. Singha, S. Mondal, T.S. Bhattacharya, L. Das, K. Sen, B. Satpati, K. Das, A. Singha, Au nanoparticles functionalized 3D-MoS2 nanoflower: an efficient SERS matrix for biomolecule sensing, Biosens. Bioelectron. 119 (2018) 10–17.
[62] E. Appah, B. Elzey, S.O. Fakayode, Investigation of the binding and simultaneous quantifications of propanil and bromoxynil herbicide concentrations in human serum albumin, J. Environ. Sci. Health. Part B 52 (2017) 495–504.
[63] O.M.A. Mbaye, A. Maroto, M.D. Gaye-Seye, L. Stephan, L. Deschamps, J.J. Aaron, P. Giamarchi, A new direct laser photo-induced fluorescence method coupled on-line with liquid chromatographic separation for the simultaneous determination of anilides pesticides, Talanta 132 (2015) 909–914.
[64] A.K. Sandhu, K. Mandal, B. Singh, Estimation and validation of propanil residues in rice and soil samples by gas liquid chromatography with electron capture detector, Bull. Environ. Contam. Toxicol. 95 (2015) 368–372.
[65] J. Filik, J.N. Harvey, N.L. Allan, P.W. May, J.E.P. Dahl, S. Liu, R.M.K. Carlson, Raman spectroscopy of diamondoids, Spectrochim. Acta, Part A 64 (2006) 681–692.
[66] K. Miyamae, M. Nakahata, Y. Takashima, A. Harada, Self-healing, expansion–contraction, and shape-memory properties of a preorganized supramolecular hydrogel through host–guest interactions, Angew. Chem. Int. Ed. 54 (2015) 8984–8987.
[67] L.-Q. Gu, S. Cheley, H. Bayley, Capture of a single molecule in a nanocavity, Science 291 (2001) 636–640.
[68] A. Michalke, A. Janshoff, C. Steinem, C. Henke, M. Sieber, H.-J. Galla, Quantification of the interaction between charged guest molecules and chemisorbed monothiolated β-cyclodextrins, Anal. Chem. 71 (1999) 2528–2533.
[69] C. Sun, S. Dudley, M. McGinnis, J. Trumble, J. Gan, Acetaminophen detoxification in cucumber plants via induction of glutathione S-transferases, Sci. Total Environ. 649 (2019) 431–439.
[70] S. Appasaheb Hapse, P. Subhash Kapare, V. Atmaram Dhumal, P. Shankar Damale, Simultaneous estimation and validation of paracetamol, chlorpheniramine maleate and phenylephrine hydrochloride in bulk and tablet dosage form by using different spectrophotometric method, Int. Res. J. Pharm. 4 (2013) 39–43.
[71] T. Madrakian, A. Afkhami, M. Mohammadnejad, Second-order advantage applied to simultaneous spectrofluorimetric determination of paracetamol and mefenamic acid in urine samples, Anal. Chim. Acta 645 (2009) 25–29.
[72] J. Esteve-Romero, J. Albiol-Chiva, J. Peris-Vicente, A review on development of analytical methods to determine monitorable drugs in serum and urine by micellar liquid chromatography using direct injection, Anal. Chim. Acta 926 (2016) 1–16.
[73] A.U. Alam, Y. Qin, M.M.R. Howlader, N.-X. Hu, M.J. Deen, Electrochemical sensing of acetaminophen using multi-walled carbon nanotube and β-cyclodextrin, Sens. Actuators, B 254 (2018) 896–909.
[74] B.B. Ivanova, Monoclinic and orthorhombic polymorphs of paracetamol—solid state linear dichroic infrared spectral analysis, J. Mol. Struct. 738 (2005) 233–238.
[75] A. Michota, J. Bukowska, Surface-enhanced Raman scattering (SERS) of 4-mercaptobenzoic acid on silver and gold substrates, J. Raman Spectrosc. 34 (2003) 21–25.
[76] C.J. Orendorff, A. Gole, T.K. Sau, C.J. Murphy, Surface-enhanced Raman spectroscopy of self-assembled Monolayers: sandwich architecture and nanoparticle shape dependence, Anal. Chem. 77 (2005) 3261–3266.